# GEO-MATERIALS:
# NON-DESTRUCTIVE EVALUATION IN GEO-SYSTEMS

D. Fratta, Civil and Env. Engineering, LSU. Baton Rouge, LA 70803
A. L. Fernández, GEOCONSULT. San Juan, PR 00936
J. C. Santamarina, Civil and Env. Engineering, Georgia Tech. Atlanta, GA 30332

**Abstract.** Soils and fractured rocks are particulate materials, i.e., their strength, stiffness and dilative/contractive behavior are controlled by the state of effective stress; in addition, fine grained particles are also affected by contact-level electrical and capillary forces. Elastic waves propagate through these materials assessing their state, without altering their properties or processes taking place within them. Furthermore, wave-based boundary measurements can be inverted to render a tomographic image of the medium. Therefore, the propagation of elastic waves opens unique possibilities for powerful research and engineering tools in geo-materials. This paper reviews the most relevant aspects of wave propagation in geo-materials, and presents two case studies in which tomographic images are obtained. The interpretation of tomographic images in terms of the stress field is discussed.

## INTRODUCTION

The non-destructive evaluation of geomaterials (soils and fracture rocks) presents unique features that are not common to other materials. In particular, the state of effective stress determines the stiffness, the strength and the dilative-contractive tendencies in particulate media. Hertz' theory predicts that two spheres made of a perfectly linear material exhibit a non-linear elastic load-deformation behavior. Furthermore, Mindlin's contact theory shows that an ensemble of particles is non-elastic [1, 2]. These two observations permit concluding that soils and rock masses are inherently non-linear and non-elastic. Furthermore, interparticle local forces (electrical and capillary) and cementation between particles affect the stiffness and the strength of geomaterials.

In addition, geomaterials are inherently multiphase, whereby the mineral skeleton coexists with the fluid phase that fills the pores. While the fluid phase has very limited effect on the shear stiffness, it may significantly affect the compressional stiffness of near-surface geomaterials. Various poroelastic effects may also develop (e.g., Biot slow P-wave and Mendel-Cryer effect).

This paper starts with a brief review of fundamental aspects of geomaterial behavior in relation to elastic wave propagation and tomographic imaging. Then, two case studies are presented to discuss the use of non-destructive evaluation techniques to obtain engineering parameters and to evaluate the behavior of earth structures in the near-surface.

## ELASTIC WAVE VELOCITY IN GEO-MATERIALS

The relevance of the state of effective stress on stiffness and velocity is addressed first, followed by a review of the implications of capillarity and cementation. Micromechanical models are invoked in this presentation.

**Effective Stress**

The longitudinal modulus E of a simple cubic packing of monosize elastic spheres subjected to isotropic effective stress σ' is [1, 2]:

$$E = \left[\frac{3 \cdot E_s^2 \cdot \sigma`}{8 \cdot \left(1 - \nu_s^2\right)^2}\right]^{1/3} \tag{1}$$

where $E_s$ and $\nu_s$ are the Young's modulus and Poisson's ratio of the material that makes the spheres. The mass density of the simple cubic packing is $\rho = \pi \cdot \rho_s / 6$ where $\rho_s$ is the density of the material that makes the spheres. Then, the P-wave velocity is:

$$V_P = \left[\frac{3 \cdot E_s^2}{8 \cdot \left(1 - \nu_s^2\right)^2}\right]^{1/6} \cdot \left[\frac{6}{\pi \cdot \rho_s}\right]^{1/2} \cdot \sigma`^{1/6} \tag{2}$$

For freshly remolded real soils and fractured rocks, predictive empirical equations are power relations such as [3, 4, 5, 6]:

$$V_P = \alpha \cdot \left(\frac{\sigma'_{\parallel}}{1\ \text{kPa}}\right)^{\beta} \tag{3}$$

$$V_S = \alpha \cdot \left(\frac{\sigma'_{\parallel}}{1\ \text{kPa}}\right)^{\beta} \cdot \left(\frac{\sigma'_{\perp}}{1\ \text{kPa}}\right)^{\chi} \tag{4}$$

or

$$V_S = \alpha \cdot \left(\frac{\sigma'_{\parallel} + \sigma'_{\perp}}{2\ \text{kPa}}\right)^{\beta} \tag{5}$$

where the α coefficient and the β exponent depend on the type of geomaterial, the nature of interparticle contacts and the stability of the granular skeleton. The β exponent varies from 0.18 for dense sands to 0.45 for highly plastic clays [7], $\sigma_{\parallel}`$ is the effective stress parallel to the direction of wave propagation, and $\sigma_{\perp}`$ is the effective stress in the direction of particle motion (S-waves). Equations 4 and 5 highlight the prevalent role of the state of stress on the polarization plane. In fact, Equation 5 suggests that the mean state of stress on the polarization plane determines the propagation velocity. A typical dataset is presented in Figure 1.

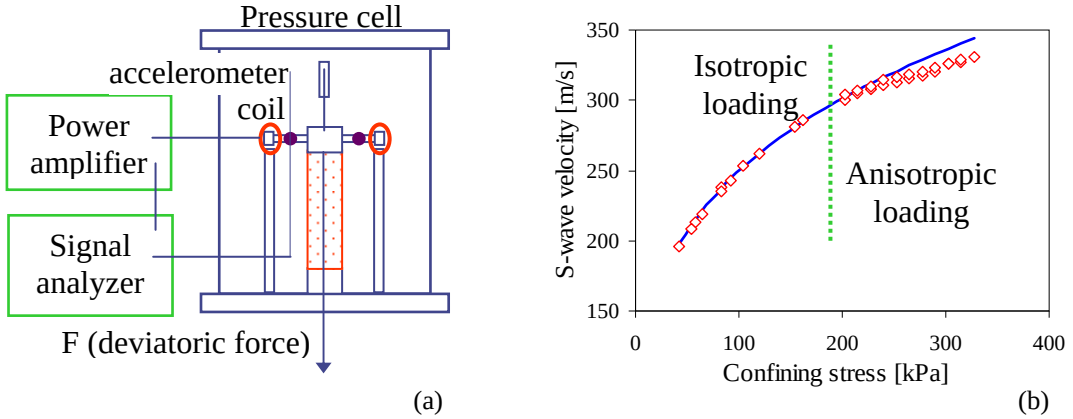


Figure 1: (a) Resonant columns tests permit measuring wave velocity and damping in geo-materials under different state of stress conditions. (b) Typical variation of S-wave velocity versus state of stress.

**Capillary**

Unsaturated conditions are always present above the free water table in the near surface. At high moisture content, the pore fluid phase is continuous (funicular regime). At low moisture content, the pore fluid form menisci at particle contacts (pendular regime). In either case, the negative pore fluid pulls particle together. The magnitude of the additional contact force in the pendular regime can be readily computed. From Lapace's equation:

$$p = T \cdot \left(\frac{1}{r_1} + \frac{1}{r_2}\right) \tag{6}$$

where p is the fluid pressure, $r_1$ and $r_2$ are the radii (see Figure 2-a), and T is the surface tension (radii have different signs). The capillary force between particles is:

$$F = p \cdot \pi \cdot {r_2}^2 \tag{7}$$

Capillary forces are most important in fine-grained soils and at low confining stress, where the contact level capillary forces may exceed the skeletal forces that carry the applied boundary stresses (Figure 2-b). As the interparticle forces increase, so does the stiffness and the wave propagation velocity.

Figure 3-a shows a soil cell with bender elements to monitor soil processes with S-waves in order to gather information about the evolution of the soil skeleton stiffness. Data in Figure 3-b corresponds to a saturated specimen of granite powder subjected to drying. When the material is fully saturated, its velocity is at a minimum (mass density is largest). As the material begins drying, the velocity increases primarily because of the decrease in mass density. As drying progresses, capillary forces develop and the shear stiffness increases. This process continues until the material approaches dry conditions. At this point, the velocity should decrease because capillary forces vanish. However, salt precipitation and the migration of fine particles to contacts render a cemented medium with high stiffness.

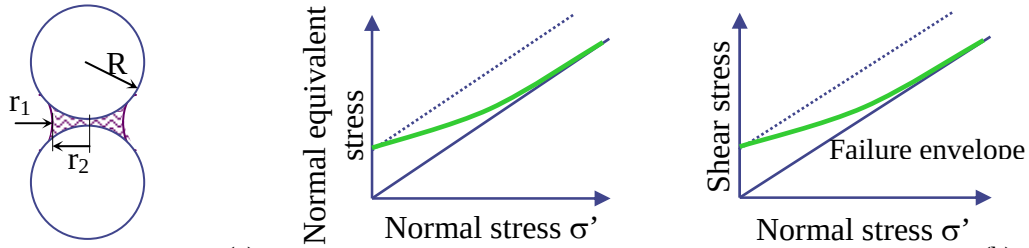


Figure 2: (a) Capillary forces between two spherical particles can be evaluated with Laplace's equation. (b) This contact-level force can be interpreted as an equivalent effective stress. It affects shear strength [8].

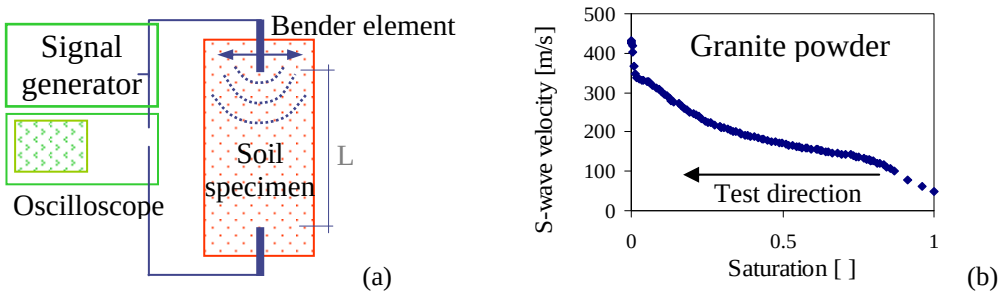


Figure 3: (a) Setup for S-wave propagation monitoring with bender elements. (b) Variation of S-wave velocity versus degree of saturation [8].

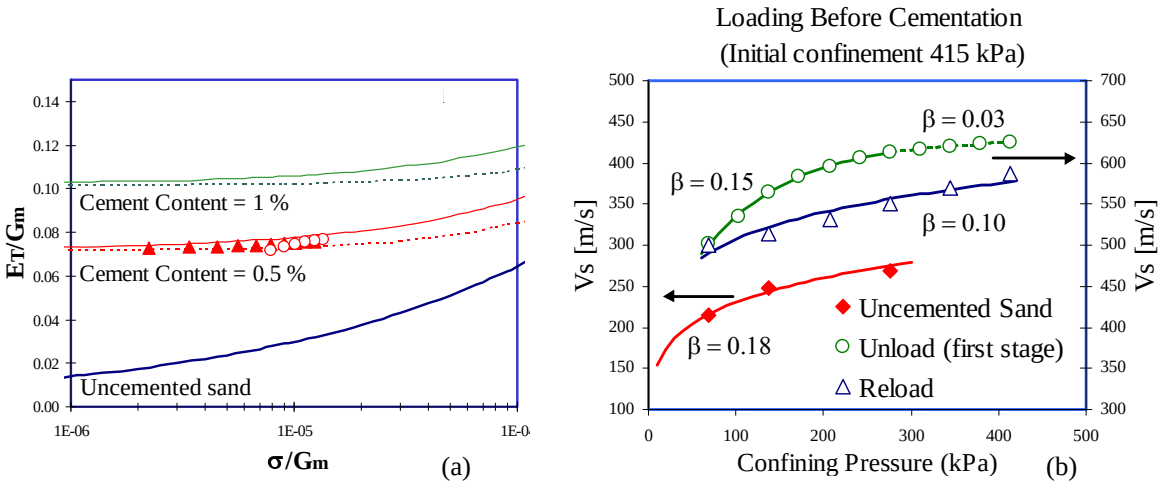


Figure 4: The effect of cementation on (a) stiffness and (b) shear wave velocity. For comparison, trends and data for uncemented sand are also presented [9].

## Cementation

Cementation can have a very important effect on the stiffness of near-surface soils, as shown in Figure 4-a (micromechanical model). As in the case of capillary forces, the effect is most evident at low confining stresses. Figure 4-b shows data for a cemented and an uncemented sand. The following observations can be made: (1) the velocity in the cemented sand is much higher; (2) the velocity in the uncemented sand is more sensitive to stress changes; (3) cementation can be lost during unloading as the strain energy stored in the soil particles is transmitted to the cementing bridges breaking them in tension.

## Heterogeneity and Anisotropy

Soil deposits are vertically heterogeneous because the effective stresses increases with depth (e.g., $\sigma'_v = \gamma \cdot z$). They are also anisotropic because the state of stress varies in the vertical plane (e.g., $\sigma'_v = k_o \cdot \sigma'_v$). While anisotropy by itself does not cause ray paths to curve, it does increase the ray curvature that develops in vertical heterogeneous media. The close-form solution for the ray path in a medium with a velocity field that increases linearly with depth and with elliptical anisotropy in the vertical plate is [10]:

$$z = \sqrt{\left(\frac{V_v^{<s>}}{b}\right)^2 + \left(x - x^{<s>}\right) \cdot \left[\frac{\left(V_v^{<r>} - V_v^{<s>}\right)^2}{b^2 \cdot \left(x^{<r>} - x^{<s>}\right)} + c^2 \cdot \left(z^{<r>} - z\right)\right]} + \frac{a}{b} \qquad (8)$$

where the superscripts s and r indicate source and receiver, and the constants a, b and c are the model parameters (Figure 5). Travel times can be computed as:

$$t = \int_s^r \frac{\partial \ell}{V_v(z,z')} = \int_s^r \frac{\sqrt{1+z'^2}}{V_v(z,z')} \cdot dx \approx \sum_{x^{<s>}}^{x^{<r>}} \frac{\sqrt{c^2+z'^2}}{(a+b\cdot z)} \cdot \Delta z \qquad (9)$$

## TOMOGRAPHIC IMAGING IN GEO-MATERIALS

Tomographic imaging is the inversion of boundary measurements to determine the velocity field within a body. This technique permits "seeing" inside the body. The travel time $t_i$ between a source and a receiver is the integral of the slowness along the ray path. If

**Model Equations:**

Vertical velocity:

$$V_v(z) = a + b \cdot z$$

Elliptical varying velocity (vertical plane):

$$V(z, z') = V_v(z) \cdot \sqrt{\frac{1+z'}{c^2+z'}}$$

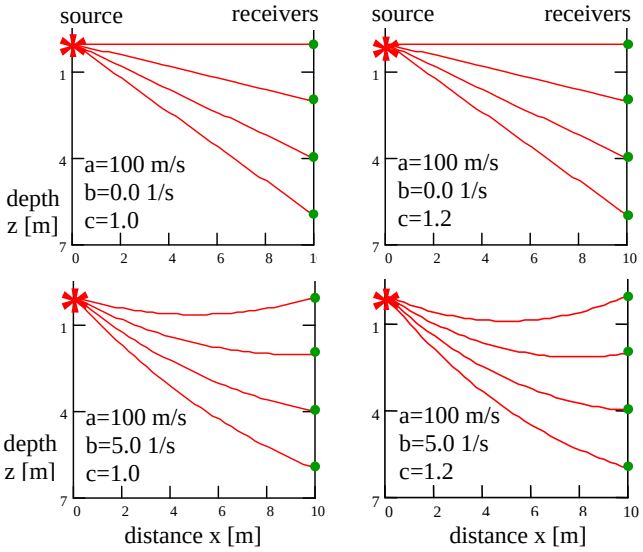


Figure 5: Effect of heterogeneity and anisotropy in ray paths.

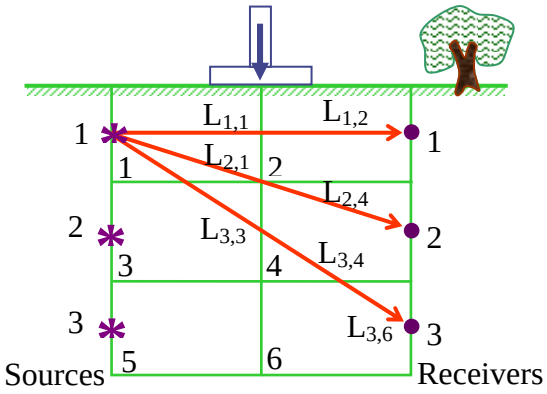


Mathematical model:

$$t_i = \sum_k \frac{L_{i,k}}{V_k} = \sum_k L_{i,k} \cdot S_k$$

$$\underline{t} = \underline{\underline{L}} \cdot \underline{S} \text{ (in matrix form)}$$

Solution:

$\underline{S} = \underline{\underline{L}}^{-g} \cdot \underline{t} \Rightarrow$ velocity field, and then image of the state of stress.

Figure 6: Pixel representation of the medium for tomographic analysis of the data.

the medium is discretized into pixels, the travel time integral can be written as a sum (Figure 6):

$$t_i = \int_s^r \frac{d\ell}{V(x,z)} \approx \sum_k \frac{L_{i,k}}{V_k} = \sum_k L_{i,k} \cdot S_k \qquad (10)$$

where $L_{i,k}$ is the distance traveled by ray i in pixel k, $V_k$ is the wave velocity at pixel k and $S_k$ is the slowness (inverse of velocity) in pixel k. Similar equations can be written for all rays. Equation 10 is a sum of products, therefore the set of equations corresponding to all rays can be arranged in matrix form as:

$$\underline{t} = \underline{\underline{L}} \cdot \underline{S} \qquad (11)$$

the travel time vector t is known, and the travel length matrix $\underline{\underline{L}}$ is computed from geometric considerations assuming the ray paths are known. The goal is to determine the slowness vector S [10]:

$$\underline{S} = \underline{\underline{L}}^{<\text{pseudo inverse}>} \cdot \underline{t} \qquad (12)$$

Once the vector S is computed, slowness values are mapped onto a color scale to render the tomographic image. Procedures that can be used to compute the pseudo inverse of $\underline{\underline{L}}$ are reviewed in the literature [10, 11].

## CASE STUDY I: KOREAN DE-MILITARIZED ZONE

This first case history is presented to demonstrate the robust evaluation of the subsurface velocity field, including its vertical heterogeneity and anisotropy. The technique is based on the parametric representation of the medium using a minimum number of parameters, and it deviates from pixel-based tomography which typically involves a large number of unknowns. The site is in the Korean Demilitarized Zone. The two boreholes are 15.2 m apart. Instrumentation involves a sparker source and a geophone. The source is activated in one borehole at 0.2 m intervals. Measurements are determined at 45, 30, 15, 0, -15, -30, and -45 degrees with respect to the horizontal. The complete data set includes a total of 1050 rays.

The data are plotted versus depth (Figure 7-a) and versus ray angle (Figure 7-b) to highlight vertical heterogeneity and anisotropy. These plots permit obtaining an initial guess of the material parameters for the model presented in Figure 5 (Equations 8 and 9).

Figure 8 shows the error-driven iterative inversion of the travel time. Two cases are considered: homogenous-isotropic and heterogeneous-anisotropic media (model in Figure 5). The $L_2$ and $L_\infty$ error norms are shown in the figure. Clearly, the heterogeneous-anistropic model yields the lowest error norm, i.e., the best prediction of the velocity field.

## CASE STUDY II: LAGUNILLAS PROTECTION DYKES

The Maracaibo lake basin lies on top of a large and shallow oil reservoir. Oil extraction has caused subsidence, thus a long dyke has been built along the shore to prevent the lake water from invading land and flooding onshore installations. The presence of the dykes

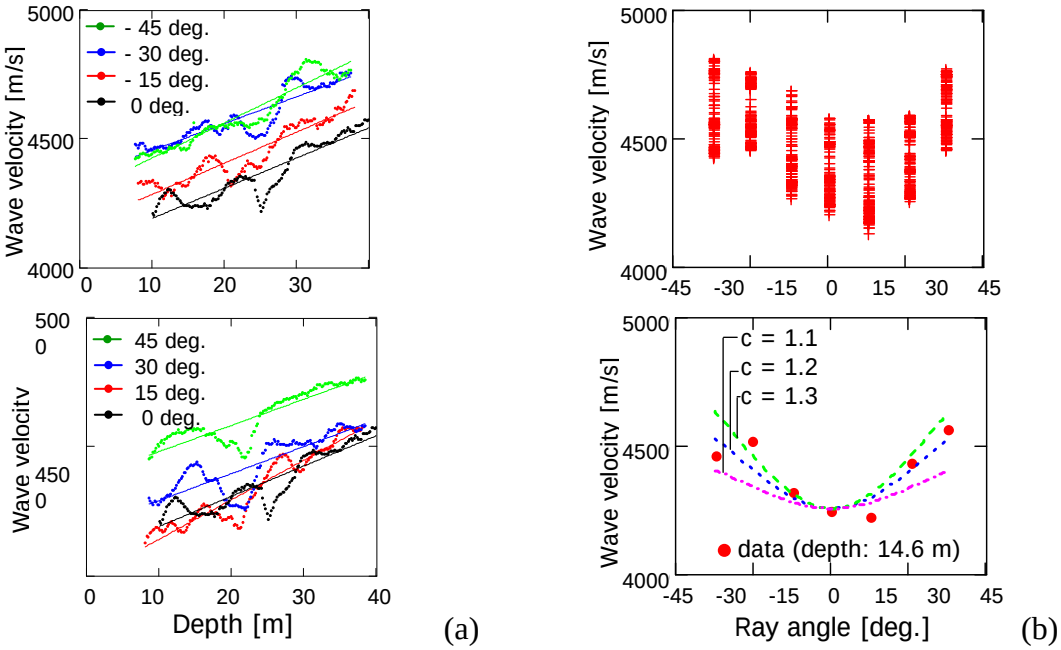


Figure 7: Tomographic data from the Korean Demilitarized Zone. (a) Effect of vertical heterogeneity on average wave velocity (straight distance divided by measured travel time). (b) Effect of stress anisotropy on average wave velocity. Model parameters are shown in Figure 5.

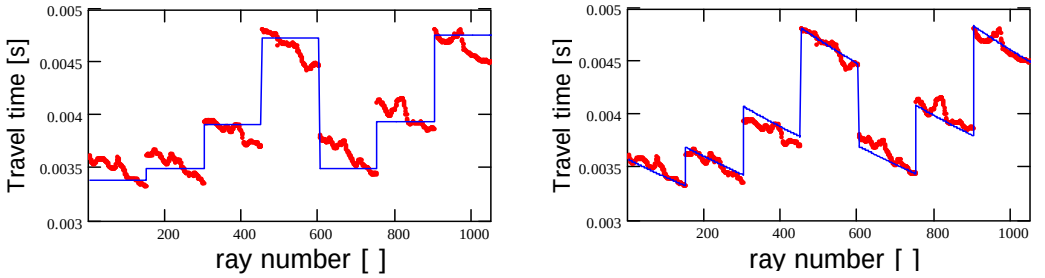


**Homogeneous and Isotropic Model**
a = 4500 m/s
b = 0 1/s
c = 1.0
$E_2$ = 3.49 % $E_\infty$ = 2.79 %

(a)

**Heterogeneous and Anisotropic Model**
a = 4560 m/s
b = 11.8 1/s
c = 1.10
$E_2$ = 1.68 % $E_\infty$ = 1.31 %

(b)

Figure 8: Tomographic inversion of cross-hole tomographic data - Korean De-militarized zone. Parametric representation of the medium according to the velocity field model shown in Figure 5.

increases the state of stress in the foundation and the contractive tendency of the soil, which may lead to liquefaction in this seismically active region. Three cross-hole geo-tomographic studies are performed at locations shown in Figure 9. The line of sources and receivers are 3 m apart. Travel time data are inverted using a pixel-based representation of the medium and presuming straight rays. The regularized least-squares solution is implemented:

$$\underline{S} = \left(\underline{\underline{L}}^{T} \cdot \underline{\underline{L}} + \lambda \cdot \underline{\underline{R}}^{-1} \cdot \underline{\underline{R}}\right)^{-1} \cdot \underline{\underline{L}}^{T} \cdot \underline{t} \qquad (13)$$

where $\lambda$ is the regularization coefficient and $\underline{\underline{R}}$ the regularization matrix. The regularization matrix permits adding a-priori information to the solution. In this case, it is assumed that the medium is horizontally smooth (Regularization based on equilibrium equations is discussed in [12]).

The computed images are presented in Figure 10. Note the low shear wave velocity under the berm (site # 2). In terms of the state of stress, these results indicate that the berm may be arching. This is an important observation for the potential long term performance of the main dyke and the protection berm. Further testing is needed to confirm this observation.

## CONCLUSIONS

- Geo-materials (soils and fractured rocks) pose unique challenges for the non-destructive evaluation of geosystems and for monitoring subsurface processes. Salient characteristics include inherent non-linear and non-elastic behavior, effective-stress dependent stiffness (and strength), and the importance of contact-level forces (capillary and electrical) particularly in near-surface soils.
- Measurements with seismic waves permit assessing the small strain stiffness, its heterogeneity and anisotropy.
- Tomographic images of shear wave velocity can be interpreted in terms of the state of the effective stress.

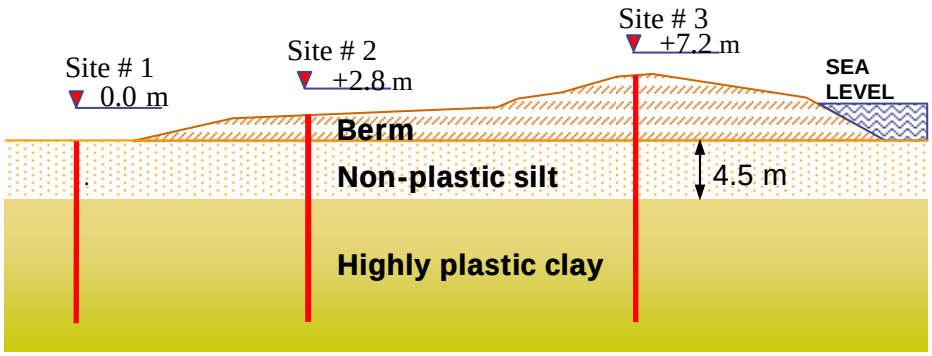


Figure 9: View of the berm, foundation soils, and site of the geo-tomography studies

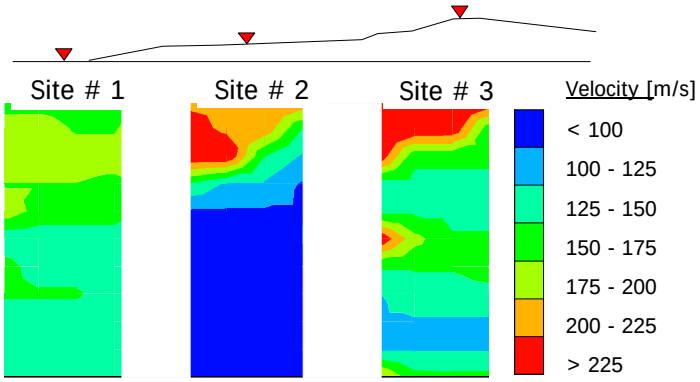


Figure 10: Images of the velocity field under the protection dyke.

## ACKNOWLEDGMENTS

This study was conducted by the authors at the Georgia Institute of Technology (School of Civil Engineering and GTREP). Support was provided by INTEVEP (Venezuela).

## REFERENCES

1. White, J. E. *Underground Sound – Application of Seismic Waves*. Elservier. Amsterdam (1981).
2. Richart, F. E., Hall, J. R., and Woods, R. D. *Vibrations of Soils and Foundations*. Prentice-Hall. Englewood, NJ (1970).
3. Roessler, S. *Journal of the Geotechnical Engineering Division* **150**, GT7, 871-880 (1979).
4. Stokoe, K.H., II, Lee, J.N.-K. and Lee, S.H.-H., "Characterization of Soil in Calibration Chambers with Seismic Waves" in *Proc. Symp. Calibration Chamber Testing*, Potsdam, N Y (1991).
5. Belloti, R., Jamiolkowski, M., Lo Presti, D.C.F. and O'Neill, D.A. *Geotechnique*, **46**, 1, 115-131 (1996).
6. Santamarina, J.C. and Cascante, G., *Canadian Geotechnical Journal*, **33**, 5, 770-782 (1996).
7. Santamarina, J.C., Klein, K. and Fam, M., *Soils and Waves* (In print), John Wiley & Sons (2001).
8. Cho, G.C. and Santamarina, J.C. *ASCE Geotechnical Journal* (In print) (2000).
9. Fernandez, A. and Santamarina, J.C., *Canadian Geotechnical Journal* (In print) (2001).
10. Santamarina, J. C. and Fratta, D., *Introduction to Discrete Signals and Inverse Problems in Civil Engineering*, ASCE Press, Reston, VA (1998).
11. Menke, W., *Geophysical Data Analysis: Discrete Inverse Theory*, Academic Press (1989).
12. Samani, A. M. W. *Travel-Time Tomography for Stress Reconstruction*. Ph.D. Thesis University of Waterloo (1997).